

## X-ray Observation of Very High Energy Gamma-ray Source, HESS J1745–303, with *Suzaku*

Aya Bamba<sup>1</sup>, Ryo Yamazaki<sup>2</sup>, Kazunori Kohri<sup>3</sup>, Hironori Matsumoto<sup>4</sup>, Stefan Wagner<sup>5</sup>,  
Gerd Pühlhofer<sup>5</sup>, Karl Kosack<sup>6</sup>

### ABSTRACT

*Suzaku* observations of a TeV unidentified (unID) source, HESS J1745–303, are presented. A possible excess of neutral iron line emission is discovered, and is likely associated with the main part of HESS J1745–303, named “region A”. It may be an X-ray reflection nebula where the X-rays from previous Galactic Center (GC) activity are reflected by a molecular cloud. This result further strengthens the assumption that the molecular cloud which is spatially coincident with region A of HESS J1745–303 is located in the GC region. The TeV emission from molecular clouds is reminiscent of the diffuse TeV gamma-rays from the GC giant molecular clouds, and it could have the same emission mechanism. With deep exposure mapping observations by *Suzaku*, a tight upper-limit on the 2–10 keV continuum diffuse emission from region A is obtained, as  $2.1 \times 10^{-13}$  ergs s<sup>-1</sup>cm<sup>-2</sup>. The flux ratio between 1–10 TeV and 2–10 keV is larger than 4. Possible scenarios to reproduce wide-band spectra from keV to TeV are examined. Thermal X-rays from nearby two old supernova remnants, G359.0–0.9 and G359.1–0.5, are detected, and their emission properties are well determined in the present study with deep exposure.

*Subject headings:* acceleration of particles — shock waves — supernova remnants — X-rays: individual (HESS J1745–303, G359.0–0.9, G359.1–0.5)

---

<sup>1</sup> ISAS/JAXA Department of High Energy Astrophysics 3-1-1 Yoshinodai, Sagami-hara, Kanagawa 229-8510, JAPAN; bamba@astro.isas.jaxa.jp

<sup>2</sup> Department of Physical Science, Hiroshima University, Higashi-Hiroshima, Hiroshima 739-8526

<sup>3</sup> Physics Department, Lancaster University, Lancaster, LA1 4YB, UK

<sup>4</sup> Department of Physics, Kyoto University, Kyoto 606-8502, Japan

<sup>5</sup> Landessternwarte, Heidelberg, Königstuhl 12, 69117, Heidelberg, Germany

<sup>6</sup> Max-Planck-Institut für Kernphysik, Heidelberg, Germany

## 1. Introduction

Very high-energy gamma-rays with energies around TeV are powerful tools to investigate the cosmic accelerators. They arise from either leptonic (cosmic microwave background (CMB) or other soft seed photons up-scattered by accelerated electrons and their bremsstrahlung emission) or hadronic (the decay of neutral pions, arising from the collision of high energy protons and interstellar matter) processes. The strong evidence for electron acceleration up to more than  $\sim 10$  TeV has been obtained with X-ray observations of, for example, young supernova remnants (SNRs) that are believed to be the most probable cosmic-ray accelerators in our Galaxy (e.g., Koyama et al. 1995, 1997; Bamba et al. 2003a,b, 2005a,b). On the other hand, we have not yet derived firm evidence for proton acceleration; although TeV gamma-rays have been detected by several of young SNRs, such as RX J1713.7–3946 (Enomoto et al. 2002; Aharonian et al. 2004a) and RX J0852.0–4622 (Katagiri et al. 2005; Aharonian et al. 2005c), their origin is not yet fully understood (e.g., Pannuti et al. 2003; Lazendic et al. 2004; Ellison 2001; Bamba et al. 2005b; Uchiyama et al. 2005, 2007; Yamazaki et al. 2008).

Recently, a survey of the inner part of our Galaxy has revealed several new TeV  $\gamma$ -ray sources (Aharonian et al. 2002, 2005a,b, 2006a). Some of them have no counterpart in the X-ray regime. Then, the flux ratio, defined by

$$R_{\text{TeV/X}} = \frac{F_{\gamma}(1 - 10 \text{ TeV})}{F_{\text{X}}(2 - 10 \text{ keV})} ,$$

is more than  $\sim 10$  (Yamazaki et al. 2006; Bamba et al. 2007; Matsumoto et al. 2007). On the other hand, young supernova remnants (SNRs) and pulsar wind nebulae have  $R_{\text{TeV/X}}$  less than  $\sim 2$ . It is interesting that the TeV unidentified sources with large  $R_{\text{TeV/X}}$  may show evidence for hadron acceleration because the leptonic inverse-Compton model requires an unusually small magnetic field strength ( $\ll 1 \mu\text{G}$ ). So far, several TeV gamma-ray objects have been followed up in X-rays, which provide us a lot of hint on the emission process of TeV gamma-rays (e.g., Tian et al. 2007; Bamba et al. 2007; Matsumoto et al. 2007, 2008).

HESS J1745–303 is one of such TeV unidentified sources. It was discovered by the Galactic plane survey of High Energy Stereoscopic System (H.E.S.S.) (Aharonian et al. 2006a), and subsequent follow-up observation was performed recently (Aharonian et al. 2008). The observed flux from the whole object is estimated as  $F_{\gamma}(1-10 \text{ TeV}) \sim 5.2 \times 10^{-12} \text{ erg s}^{-1} \text{ cm}^{-2}$ . The low Galactic latitude and the fact that the source is spatially extended strongly argues for a Galactic origin of HESS J1745–303. HESS J1745–303 mainly consists of three bright emission regions (named region A, B, and C; Aharonian et al. 2008), and the angular size of the whole object is  $\sim 0.3^{\circ} \times 0.5^{\circ}$ , which is one of the largest TeV unID sources. HESS J1745–303 has direct positional coincidence with an unidentified

EGRET source (3EG J1744–3011, Hartman et al. 1999), which implies proton acceleration because the leptonic IC model for the TeV emission usually predict very dim GeV  $\gamma$ -rays. Aharonian et al. (2008) suggested that a molecular cloud coincides with the TeV emitting region, although the precise distance to the molecular cloud is unknown. This region was also observed with *XMM-Newton*, which gives an upper-limit on the diffuse X-ray emission,  $4.5 \times 10^{-13}$  erg cm $^{-2}$ s $^{-1}$ , from the region A which is the main part of HESS J1745–303 and has a TeV energy flux of  $8.0 \times 10^{-13}$  erg cm $^{-2}$ s $^{-1}$ . Then, the TeV-to-X-ray flux ratio,  $R_{\text{TeV}/\text{X}}$ , is larger than  $\sim 2$ .

In this paper, we report on the deep mapping observations of HESS J1745–303 with X-ray satellite *Suzaku* (Mitsuda et al. 2007). Section 2 introduces the observations. Our analysis is explained in § 3, and we discuss our findings in § 4.

## 2. Observations and Data Reduction

We carried out mosaic observations of HESS J1745–303 with *Suzaku*. The mapping used four pointings as listed in Table 1. *Suzaku* has two active instruments, four X-ray Imaging Spectrometers (XIS0–XIS3; Koyama et al. 2007) each at the focus of an X-Ray Telescope (XRTs Serlemitsos et al. 2007) and a separate Hard X-ray Detector (HXD; Takahashi et al. 2007). All four spectrometers were active in the first observation, whereas only three could be used subsequently due to a problem with XIS 2. XIS1 is a back-illuminated (BI) CCD, whereas the others are front-illuminated (FI). The XIS was operated in the normal full-frame clocking mode. The spaced-row charge injection (Nakajima et al. 2008) was used in the later three observations (Table 1). The data reduction and analysis were made using HEADAS software version 6.4., version 2.2.7.18 of the processed data, and XSPEC version 11.3.2. We filtered out data obtained during passages through the South Atlantic Anomaly (SAA), with elevation angle to the Earth’s limb below  $5^\circ$ , or with elevation angle to the bright Earth’s limb below  $13^\circ$ . in order to avoid the contamination of emission from the bright Earth. In this paper, we concentrate on the XIS data analysis, because HESS J1745–303 is located near the Galactic plane, and the HXD data is contaminated by the Galactic ridge X-ray emission (GRXE; c.f., Koyama et al. 1989; Yuasa et al. 2007) and bright point sources, which are quite difficult to remove correctly.

### 3. Results

#### 3.1. Images

We made mosaic intensity maps in the 0.5–2.0 keV, 2.0–8.0 keV, and 6.3–6.5 keV bands of the four pointing observations as described in the following.

The raw mosaic images were made in each energy band. In order to estimate the continuum emission in the narrow iron intensity band, we derived the spectrum over the entire region and fitted 3–8 keV photons with a power-law plus narrow Gaussians which represent emission lines. The 2–3 keV band photons were not used in order to avoid the influence of soft discrete emission (two SNRs; described later). The best-fit photon index was  $\sim 1 - -1.3$ . We compared the count rates of the power-law component in the 2.0–8.0 keV and 6.3–6.5 keV bands, the latter is 1.15% of the former, and normalized the 2.0–8.0 keV image with the ratio. The normalized continuum image was subtracted from the 6.3–6.5 keV image, which is the “neutral iron intensity image”.

The non-X-ray background (NXB) image for each energy band was generated from the NXB database provided by the Suzaku team. The NXB images were chosen to make the average geomagnetic cu-off rigidity same as that of the observation, and extracted from the same region in the detector. In this procedure, `xisnxbgen` package developed by Tawa et al. (2008) was used. After subtracting NXB images from the raw images, we combined the NXB-subtracted images using `ximage` package.

The exposure maps were made for 0.5–2.0 and 2.0–8.0 keV bands with the `xissim` package (Ishisaki et al. 2007). For the neutral iron line map, the 2.0–8.0 keV energy range was used. The exposure maps were also combined. Dividing the NXB-subtracted images with the exposure maps, we made the mosaic images shown in Figure 1. Our observations cover all of the region A of HESS J1745–303 .

On the eastern edge of HESS J1745–303 , we can see some diffuse components in the soft X-ray band, (see Figure 1(a)). They coincide with two radio SNRs, G359.0–0.9 and G359.1–0.5 (LaRosa et al. 2000; Bamba et al. 2000). Some point sources are also seen, as reported by Aharonian et al. (2008). However, no excess was found within the HESS J1745–303 region. The hard band image (Figure 1b) also shows no diffuse source. In the neutral iron line map (Figure 1c), on the other hand, some excess is shown around region A.

## 3.2. Spectra

### 3.2.1. The X-ray spectrum of the region A

We selected source and background regions (“Src” and “Bgd1–3” hereafter) as shown with solid lines in Figure 2, to make the upper-limit of the X-ray emission of HESS J1745–303 region A. The background regions were divided to 3 regions (Bgd1–3 in Figure 2). Two types of background should be considered, NXB and the GRXE (Yamauchi & Koyama 1993, for example). The latter has positional dependence along the Galactic longitude. We thus used Bgd1 and 2 regions to make the average longitude of each region similar. The 3–8 keV count rates of XIS 0 are  $(6.0 \pm 0.05) \times 10^{-4}$  and  $(7.0 \pm 0.1) \times 10^{-4}$  cnts s<sup>-1</sup>arcmin<sup>-2</sup> for the source and the background regions, respectively. For making the upper-limit of the X-ray flux in the source region, the response and auxiliary files were constructed using `xisrmfgen` and `xissimarfgen` (Ishisaki et al. 2007) in the HEADAS package, with the assumption that the emission comes from the source region uniformly. The photons from the background regions were subtracted from the source spectra. We fit the background-subtracted spectra in the 2–10 keV band with a power-law model with fixed  $\Gamma = 2$ , which is significantly harder value than the TeV emission (Aharonian et al. 2008), and to derive the 90% upper-limit of  $2.1 \times 10^{-13}$  ergs cm<sup>-2</sup>s<sup>-1</sup>. The larger photon indices were also used to estimate the systematic errors of the upper-limit and derived the smaller value.

We also derived the surface brightness of the neutral iron emission line in each region. Only the FI CCD data were used since the BI CCD has larger background in the hard X-ray band. We fitted 5–8 keV spectra with a power-law component, narrow Gaussians for neutral, He-like, and H-like iron lines, and for Mn-K, and Ni-K lines as NXB emission. The best-fit models and parameters of the neutral and He-like iron lines in each region are shown in Figure 3 and Table 2. The surface brightness of He-like iron is almost constant between these regions. We added all background regions to increase statistics and derived the average values of line intensity. After the procedure, the neutral iron line is significantly stronger in the source region than those in background regions, whereas the He-like iron line is compatible in both regions. The total excess of the line in these regions is  $1.1 \times 10^{-5}$  ph s<sup>-1</sup>cm<sup>-2</sup>.

### 3.2.2. G359.0–0.9 and G359.1–0.5

For the spectral analysis of the two SNRs, we used the regions with dashed-lines in Figure 2. Background photons were accumulated from the source-free regions in the same observation. The background-subtracted spectra are shown in Figure 4. The spectra are rather soft and there are emission lines from highly ionized Si and S in both spectra. These

facts indicate that these emissions are thermal, which is consistent with the *ASCA* results (Bamba et al. 2000). We then fitted these spectra with non-equilibrium ionization collisional plasma model (`nei` in XSPEC; Borkowski et al. 2001) with absorption. For the absorption model, we used the cross sections of Morrison & McCammon (1983) and assumed solar abundances (Anders & Grevesse 1989). The XIS team reported the gain uncertainty of a few eV (c.f., Koyama et al. 2007), thus the gain is allowed to vary within a few percent separately. Bamba et al. (2000) reported that the spectrum of G359.1–0.5 was well described with the two-temperature model with high-S abundance in the higher temperature component. So we have added another thermal component in the present analysis. We treated some abundances in Table 3 as free parameters and fixed the others at 1 solar. The best-fit models and parameters are shown in Figure 4 and Table 3.

The results are consistent with the *ASCA* results, but the abundance and the ionization time scale are better determined thanks to the better energy resolution of XIS. We expect a difference in flux, since our observations do not cover the entire remnants. The absorption column of G359.0–0.9 is smaller than sources in the Galactic center (GC), thus this SNR is likely a foreground source. On the other hand, G359.1–0.5 shows a very large absorption column, which implies that it is in the GC region.

## 4. Discussion

### 4.1. The neutral iron line and molecular clouds

Aharonian et al. (2008) reported that HESS J1745–303 region A had spatial coincidence with a molecular cloud (Bitran et al. 1997). We suggest that the TeV emission is also associated with the neutral iron line emission, although we cannot unambiguously conclude that due to the poor statistics. The positional coincidence of the neutral iron line and the molecular cloud reminds us of reflected X-rays originating in the past activity in the GC (e.g., Inui et al. 2008). If the molecular cloud is optically thin, the line emission intensity,  $I_{\text{Fe}}$ , should be proportional to the mass of the molecular cloud and the viewing angle from the GC, so that

$$I_{\text{Fe}} \propto \frac{M_{\text{MC}}}{(D\theta)^2} ,$$

where  $M_{\text{MC}}$ ,  $\theta$ , and  $D$  are the mass of the molecular cloud, the angular size of the molecular cloud viewed from the GC, and the angular separation between the cloud and the GC, respectively (Nobukawa et al. 2008). We compared the masses of the molecular cloud coincident with source A of HESS J1745–303 and the most famous X-ray reflection nebula, Sgr B2 (Murakami et al. 2001). The latter shows neutral iron line emission with an intensity

of  $5.6 \times 10^{-5} \text{ ph s}^{-1} \text{ cm}^{-2}$ . Table 4 shows the characteristics of these molecular clouds. For the molecular cloud at region A of HESS J1745–303, we obtain  $I_{\text{Fe}} \sim 7 \times 10^{-6} \text{ ph s}^{-1} \text{ cm}^{-2}$  on the assumption of time-independent ejected X-ray luminosity at the GC. This estimated value is compatible with the observed one,  $1.1 \times 10^{-5} \text{ ph s}^{-1} \text{ cm}^{-2}$ . Therefore, we conclude that this molecular cloud is a new example of X-ray reflection nebula and that the molecular cloud is located in the GC region. We believe that hard X-ray observations are the strong tools to judge whether the molecular clouds are in the GC region or not.

#### 4.2. The upper-limit of the nonthermal Component of X-rays and Possible Emission Mechanism of TeV Gamma-rays

We derive a 90% X-ray flux upper-limit for the HESS J1745–303 region A in the 2–10 keV band of  $2.1 \times 10^{-13} \text{ ergs s}^{-1} \text{ cm}^{-2}$ , which is tighter than the *XMM* results (Aharonian et al. 2008). The flux ratio between 2–10 keV and 1–10 TeV,  $R_{\text{TeV}/\text{X}}$ , is larger than 4, which could be larger than TeV emitting shell-type SNRs and PWNe (Bamba et al. 2007; Matsumoto et al. 2007; Yamazaki et al. 2006).

In the following, we discuss specific models of the emission mechanism to reproduce the observed results of X-ray and TeV gamma-rays for the region A of HESS J1745–303. In particular, we focus on whether or not the upper limit of nonthermal X-ray emission, which is derived in the present work, gives us significant constraints on the theoretical models. We consider hadronic and leptonic models separately. Since HESS J1745–303 is near the Galactic center, the GeV emission may be overlaid with the intense Galactic diffuse emission and uncertainty is very large. Hence we neglect it here for simplicity, and take into account only X-ray and TeV gamma-ray bands.

##### 4.2.1. Hadronic gamma-ray emission model

In hadronic models, TeV gamma-rays originate from accelerated protons. It is assumed that the proton energy spectrum has a form of  $E^{-p} \exp(-E/E_{\text{max},p})$  with an index,  $p$ , and cut-off energy,  $E_{\text{max},p}$ . Here, the value of  $p$  is highly uncertain, so we adopt  $p = 2$  as a typical value. The high-energy protons collide with target protons in the ISM or molecular cloud, generating neutral ( $\pi^0$ ) and charged ( $\pi^\pm$ ) pions. The former decays into gamma rays, while the decay of the latter causes secondary electrons and positrons producing bremsstrahlung, inverse Compton, and synchrotron emission.

Although it may be likely that the region A of HESS J1745–303 is associated with a

molecular cloud and target matter density  $n$  is high, the low- $n$  case cannot be, at present, excluded. So, we consider two cases, in which  $n = 1 \text{ cm}^{-3}$  and  $n = 5 \times 10^3 \text{ cm}^{-3}$ , independently. The value of  $n$  in the latter case is adopted according to Aharonian et al. (2008). Generally speaking, in the former, bremsstrahlung emission is not dominant in the TeV gamma-ray band, while it may often be dominant in the latter.

At first we consider the case  $n = 1 \text{ cm}^{-3}$  (see the left panel of Fig. 5). Since the value of  $n$  is small, emissions from secondary electrons is dim in the gamma-ray band, so that the  $\pi^0$ -decay emission dominates. We find that as long as  $n \lesssim 10^2 \text{ cm}^{-3}$ , the bremsstrahlung emission of secondary electrons and positrons is not dominant in the gamma-ray band. We fix  $E_{\text{max,p}} = 18 \text{ TeV}$  in order to fit the observed spectral shape in the TeV energy range. Then, as can be seen in the left panel of Fig. 5, derived upper limit on nonthermal X-rays are explained if the magnetic field  $B \lesssim 100 \text{ mG}$ . This is rather loose limit on the magnetic field. Because of the small value of  $E_{\text{max,p}}$ , the maximum energy of secondary electrons and positrons is small,  $\sim 1 \text{ TeV}$ , so that the large value of  $B$  is necessary for bright synchrotron X-rays emitted by them. This comes from the fact that the characteristic frequency of electron/positron synchrotron radiation is given by

$$h\nu_{\text{syn}} \sim 6 \text{ keV} \left( \frac{B}{50 \text{ mG}} \right) \left( \frac{E_{e^\pm}}{1 \text{ TeV}} \right)^2 ,$$

where  $E_{e^\pm}$  is the energy of secondary electrons or positrons. For assumed distance of 8.5 kpc, the total energy of accelerated protons is estimated as  $\sim 6 \times 10^{50} \text{ erg}$ .

Next we consider the case  $n = 5 \times 10^3 \text{ cm}^{-3}$  (see the right panel of Fig. 5). If the magnetic field strength is small ( $B \lesssim 10^2 \mu\text{G}$ ), the bremsstrahlung emission from secondary electrons and positrons is comparable to the  $\pi^0$ -decay gamma-ray emission. However, in the strong field cases, the synchrotron cooling effect significantly suppresses the number of  $e^\pm$ , resulting small contribution to the gamma-rays. On the other hand, the synchrotron radiation of secondary  $e^\pm$  is brighter for larger  $B$ . Similar to the case of  $n = 1 \text{ cm}^{-3}$ , the magnetic field is no larger than  $\sim 100 \text{ mG}$ . Robinson et al. (1996) derived the relatively high magnetic field value, 0.2–0.6 mG, which is measured from the Zeeman splitting of maser lines. The molecular cloud associated with the region A might have the similar magnetic field strength, and then,  $\sim \text{mG}$  field and the number density of the cloud  $n \sim 5 \times 10^3 \text{ cm}^{-3}$  is roughly consistent with the previous result on other molecular clouds (Crutcher 1991). As long as the field strength in the cloud is  $B \sim \text{mG}$  or less, the expected flux of secondary synchrotron radiation in the X-ray band is rather small and below the observed upper limit. For assumed distance of 8.5 kpc, the total energy of accelerated protons is estimated as  $\sim 1.2 \times 10^{47} \text{ erg}$ . Then, the mean energy density of high-energy protons at region A of HESS J1745–303 is calculated as  $\sim 6.0 \text{ eV cm}^{-3}$  if we assume the volume of the molecular



cloud of  $1.2 \times 10^{58} \text{ cm}^3$  (Aharonian et al. 2008),

#### 4.2.2. Leptonic gamma-ray emission model

In the leptonic model, TeV gamma-rays arise via bremsstrahlung and inverse Compton process (with CMB seed photons) emissions of primarily accelerated electrons, and X-rays arise from their synchrotron radiation. Again we assume that the electron energy spectrum has a form of  $E^{-p} \exp(-E/E_{\text{max,e}})$  with an fixed index,  $p = 2.0$ , and the cut-off energy,  $E_{\text{max,e}}$ . As well as the hadronic model, both low- and high- $n$  cases are discussed.

First we consider the case  $n = 0.1 \text{ cm}^{-3}$  (see the left panel of Fig. 6). In this case, the TeV gamma-ray band is dominated by the IC emission. In order to explain the observed hard TeV spectrum, we adopt  $E_{\text{max,e}} = 10 \text{ TeV}$ . Then, the relatively weak magnetic field,  $B \lesssim 6 \mu\text{G}$ , is necessary in order for the flux of synchrotron X-rays to be smaller than the observed upper limit. We find that for an assumed distance of 8.5 kpc, the total energy of accelerated electrons is estimated as  $\sim 6 \times 10^{48} \text{ erg}$ , which is very large compared with the typical young SNRs (e.g., Bamba et al. 2003b).

Next we consider the case  $n = 5 \times 10^3 \text{ cm}^{-3}$  (see the right panel of Fig. 6). In this case, the TeV gamma-ray band is dominated by the bremsstrahlung emission. When the magnetic field is larger than  $\sim 100 \mu\text{G}$ , the synchrotron cooling effect is significant and the electron spectrum is modified enough for the emission spectrum in the TeV gamma-ray band to deviate from the observed one. As long as  $B \lesssim 10^2 \mu\text{G}$ , we can fit the TeV gamma-ray spectrum with bremsstrahlung emission, and the synchrotron X-rays below the observed upper limit. For assumed distance of 8.5 kpc, the total energy of accelerated electrons is estimated as  $\sim 6.0 \times 10^{45} \text{ erg}$  and  $\sim 2.3 \times 10^{46} \text{ erg}$  for  $B = 10 \mu\text{G}$  and  $B = 100 \mu\text{G}$ , respectively. If we assume the volume of the molecular cloud of  $1.2 \times 10^{58} \text{ cm}^3$  (Aharonian et al. 2008), the mean energy density of high-energy protons at region A of HESS J1745–303 is calculated as  $\sim 0.31 \text{ eV cm}^{-3}$  and  $\sim 1.2 \text{ eV cm}^{-3}$  for  $B = 10 \mu\text{G}$  and  $B = 100 \mu\text{G}$ , respectively.

In the case of  $n = 5 \times 10^3 \text{ cm}^{-3}$ , the energy-loss time scale,  $t_{\text{loss}}$ , for TeV-emitting electrons via synchrotron and bremsstrahlung radiation is less than  $\sim 3 \times 10^3 \text{ yr}$ . Then, the diffusion length scale is estimated as  $\sqrt{2Kt_{\text{loss}}} \lesssim 0.26\eta^{1/2}(B/10 \mu\text{G})^{-1/2}(E_e/\text{TeV})^{1/2} \text{ pc}$ , where we assume the Bohm type diffusion,  $K = cE_e\eta/3eB$ . Even if  $\eta \sim 10^2$ , this length scale is much smaller than the source size of region A of HESS J1745–303 ( $\sim 40 \text{ pc}$  assuming the distance of 8.5 kpc), which implies that the high-energy electrons coming from a nearby accelerator cannot penetrate into deep interior of a molecular cloud. On the other hand,

when  $n = 0.1 \text{ cm}^{-3}$ , relatively large energy of accelerated electrons is required. So, the leptonic models considered above may be unlikely. However, in order to derive the firm conclusion, we need to discuss further detail with more information on HESS J1745–303, such as the intrinsic source size, the number density of target matter, more precise spectrum in all wavelength (from radio to GeV–TeV gamma-rays), and so on.

### 4.3. Source of High Energy Particles

Spatial coincidence of a molecular cloud and the TeV gamma-rays at region A of HESS J1745–303 suggests that the TeV emission is possibly due to accelerated protons interacting the molecular cloud. The source of high energy protons is still unknown. The past GC activity might be able to make protons (Aharonian et al. 2006b). However, it is rather difficult due to the low mass of the molecular cloud in our region. Nearby SNRs and pulsars, on the other hand, could be high-energy proton injectors. G359.1–0.5 is an energetic SNR and interacting with the molecular cloud (Uchida et al. 1992) and is located in the GC region. We confirmed that the distances to this SNR and the molecular clouds are similar, but we could not find any signature of the interaction in X-rays. Hidden SNRs by the molecular cloud also could be the source of accelerated particles. The average absorption column of the molecular cloud is  $\sim 10^{23} \text{ cm}^{-2}$ , which is enough to hide the soft X-ray emission from the SNRs. For further study, more detailed radio observations are needed. G359.0–0.9 is an unrelated source with its significantly smaller distance (Bamba et al. 2000). A pulsar B1742–30 has been argued as a possible cosmic ray injector (e.g., Lemièrre et al. 2007), but the estimated distance (2.1 kpc; Taylor et al. 1993) is significantly smaller than that of HESS J1745–303. We thus concluded that the pulsar B1742–30 is also unrelated to HESS J1745–303.

## 5. Summary

Deep mapping observations of a part of HESS J1745–303 have been carried out with *Suzaku*. The main part of HESS J1745–303, region A, is entirely covered in the present observation. We made a tight upper limit of hard X-rays of the HESS J1745–303 region,  $2.1 \times 10^{-13} \text{ ergs s}^{-1} \text{ cm}^{-2}$  in the 2–10 keV band. The flux ratio between 1–10 TeV and 2–10 keV is larger than 4, which could make HESS J1745–303 one of the “dark particle accelerators”. An excess of the neutral iron emission line on this region is found. This possible excess should be due to the X-ray reflection from a molecular cloud by the past active GC. This provides strong evidence for the interaction between the molecular cloud —

HESS J1745–303 system in the GC region. With the small flux in the hard X-ray band and coincidence with a molecular cloud, the TeV emission from HESS J1745–303 could be due to protons encountered the molecular cloud.

We would like to thank the referee for useful comments and suggestions. The authors also thank H. Murakami, A. Kawachi, T. Oka, and Y. Fukui, for their useful comments on molecular clouds and X-ray reflection nebulae. This work was supported in part by Grant-in-Aid for Scientific Research of the Japanese Ministry of Education, Culture, Sports, Science and Technology, No. 19·4014 (A. Bamba), No. 18740153 and No. 19047004 (R. Yamazaki), and also supported in part by PPARC grant, PP/D000394/1, EU grant MRTN-CT-2006-035863, the European Union through the Marie Curie Research and Training Network “UniverseNet”, MRTN-CT-2006-035863 (K. Kohri).

## REFERENCES

- Aharonian, F. et al., 2002, *A&A*, 393, L37
- Aharonian, F. et al., 2004a, *Nature*, 432, 75
- Aharonian, F. et al., 2005a, *Science*, 307, 1938
- Aharonian, F. et al., 2005b, *A&A*, 439, 1013
- Aharonian, F. et al., 2005c, *A&A*, 437, L7
- Aharonian, F. et al., 2006a, *ApJ*, 636, 777
- Aharonian, F., et al. 2006b, *Nature*, 439, 695
- Aharonian, F., et al. 2008, *A&A*, 483, 509
- Anders, E., & Grevesse, N. 1989, *Geochim. Cosmochim. Acta*, 53, 197
- Bamba, A., Yokogawa, J., Sakano, M., & Koyama, K. 2000, *PASJ*, 52, 259
- Bamba, A., Ueno, M., Koyama, K., Yamauchi, S., 2003a, *ApJ*, 589, 253
- Bamba, A., Yamazaki, R., Ueno, M., Koyama, K., 2003b, *ApJ*, 589, 827
- Bamba, A., Yamazaki, R., Yoshida, T., Terasawa, T., Koyama, K., 2005a, *ApJ*, 621, 793
- Bamba, A., Yamazaki, R., Hiraga, J., 2005b, *ApJ*, 632, 294

- Bamba, A. et al., 2007, PASJ, 59, S209
- Bitran, M., Alvarez, H., Bronfman, L., May, J., & Thaddeus, P. 1997, A&AS, 125, 99
- Borkowski, K.J., Lyerly, W.J., & Reynolds, S.P. 2001a, ApJ, 548, 820
- Crutcher, R. M. 1991, ApJ, 520, 706
- Ellison, D. C., 2001, PTPS, 143, 125
- Enomoto, R. et al. 2002, Nature, 416, 823
- Hartman, R. C. et al. 1999, ApJS, 123, 79
- Inui, T., Koyama, K., Matsumoto, H., & Tsuru, T. G. 2008, ArXiv e-prints, 803, arXiv:0803.1528
- Ishisaki, Y. et al. 2007, PASJ, 59, S113
- Katagiri, H. et al., 2005, ApJ, 619, L163
- Koyama, K., Awaki, H., Kunieda, H., Takano, S., & Tawara, Y. 1989, Nature, 339, 603
- Koyama, K., Petre, R., Gotthelf, E.V., Hwang, U., Matura, M., Ozaki, M., & Holt S.S. 1995, Nature, 378, 255
- Koyama, K. et al. 1997, PASJ, 49, L7
- Koyama, K. et al. 2007, PASJ, 59, S23
- LaRosa, T. N., Kassim, N. E., Lazio, T. J. W., & Hyman, S. D. 2000, AJ, 119, 207
- Lazendic J. S., Slane P. O., Gaensler B. M., Reynolds S. P., Plucinsky P. P., Hughes J. P., 2004, ApJ, 602, 271
- Lemiere, A. et al. 2007, in proc. of 30th Int. Cosmic Ray Conf. (Mexico), (p.42 in arXiv:0710.4057)
- Murakami, H., Koyama, K., & Maeda, Y. 2001, ApJ, 558, 687
- Roberts, M. S. E., Romani, R. W., & Kawai, N. 2001, ApJS, 133, 451
- Matsumoto, H. et al. 2007, PASJ, 59, S199
- Matsumoto, H. et al. 2008, PASJ, 60, S163

- Mitsuda, K. et al. 2007, PASJ, 59, S1
- Morrison, R., & McCammon, D. 1983, ApJ, 270, 119
- Nakajima, H. et al. 2008, PASJ, 60, S1
- Nobukawa, M., et al. 2008, PASJ, 60, 191
- Pannuti, T. G., Allen, G. E., Houck, J. C., & Sturmer, S. J., 2003, ApJ, 593, 377
- Robinson, B. Yusef-Zadeh, F., & Roberts, D. 1996, Bull. Am. Astron. Soc., 28, 948
- Serlemitsos, P. et al. 2007, PASJ, 59, S9
- Takahashi, T. et al. 2007, PASJ, 59, S35
- Tawa, N., et al. 2008, PASJ, 60, 11
- Taylor, J. H., Manchester, R. N., & Lyne, A. G. 1993, ApJS, 88, 529
- Tian, W. W. et al. 2007, ApJ, 657, L25
- Uchida, K., Morris, M., & Yusef-Zadeh, F. 1992, AJ, 104, 1533
- Uchiyama, Y., Aharonian, F. A., Takahashi, T., Hiraga, J. S., Moriguchi, Y., & Fukui, Y., 2005, in Proc. of International Symposium on High Energy Gamma-ray Astronomy, Heidelberg, July 2004 (astro-ph/0503199)
- Uchiyama, Y., Aharonian, F. A., Tanaka, T., Takahashi, T., & Maeda, Y. 2007, Nature, 449, 576
- Yamauchi, S., & Koyama, K. 1993, ApJ, 404, 620
- Yamazaki, R. et al. 2006, MNRAS, 371, 1975
- Yamazaki, R. et al. 2008, arXiv:0806.3303
- Yuasa, T. et al. 2007, PASJ, in press

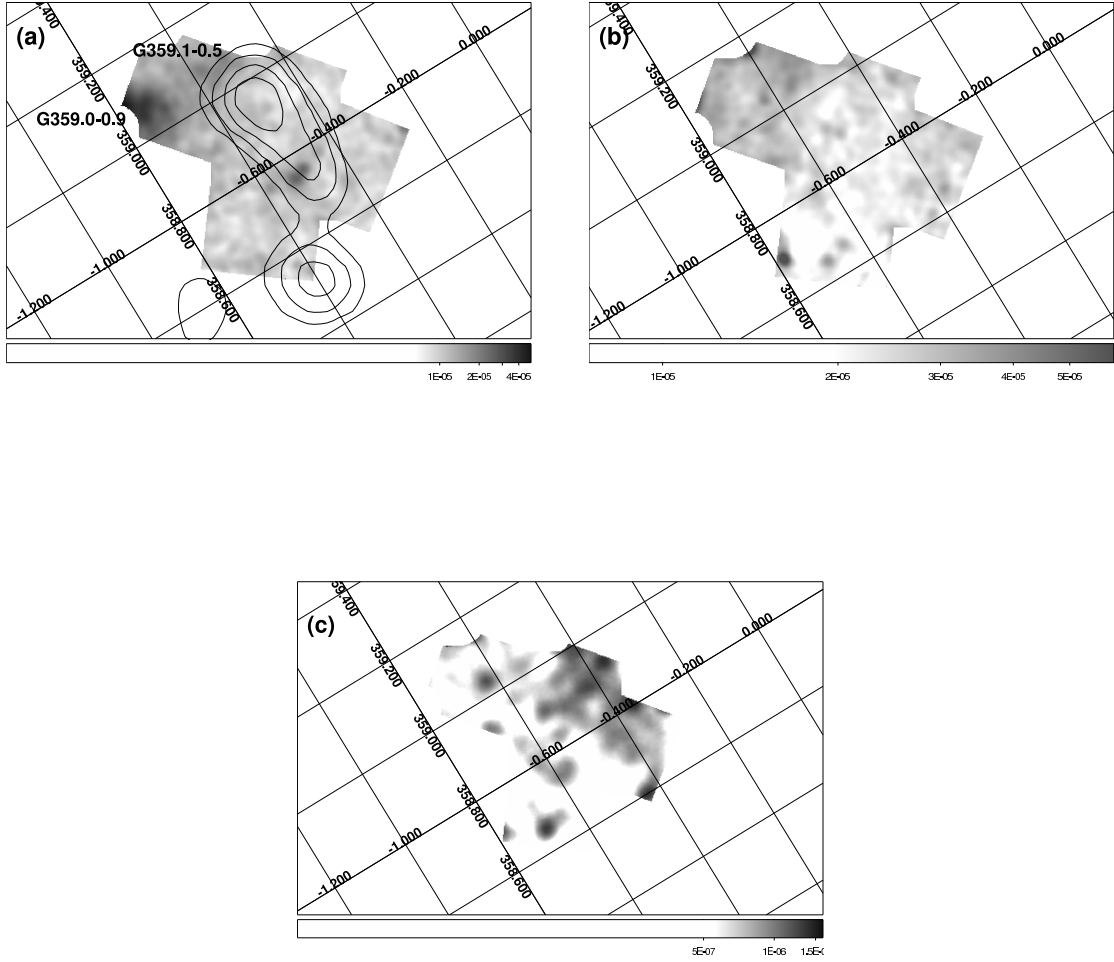


Fig. 1.— *Suzaku* XIS intensity maps of the HESS J1745–303 region in the 0.5–2.0 keV (a) and 2.0–8.0 keV (b) bands, and the neutral iron line (c). The scale is in the logarithmic. The contour represents TeV emission in the linear scale.

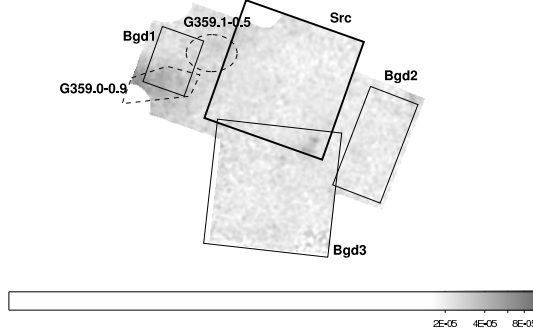


Fig. 2.— Regions for the spectral analysis overlaid on the 0.5–2.0 keV image. Thick and thin solid rectangles are source and background regions for the HESS J1745–303 region analysis. Dashed regions are for G359.0–0.9 and G359.1-0.5 analysis.

Table 1. Observation Log

| ObsID               | Date<br>YYYY-MM-DD | Position<br>(J2000) | Exposure<br>[ksec] | SCI |
|---------------------|--------------------|---------------------|--------------------|-----|
| 501010010 . . . . . | 2006-10-07         | (266.26, –30.37)    | 53                 | OFF |
| 502016010 . . . . . | 2008-03-02         | (266.22, –30.11)    | 73                 | ON  |
| 502017010 . . . . . | 2008-03-06         | (266.47, –30.09)    | 75                 | ON  |
| 502018010 . . . . . | 2008-03-08         | (266.06, –30.24)    | 82                 | ON  |

Table 2. Comparison of The Iron Emission Lines

|  | Src              | Bgd1            | Bgd2             | Bgd3             | Bgd average      |
|--|------------------|-----------------|------------------|------------------|------------------|
| Neutral Iron   |                  |                 |                  |                  |                  |
| Line center [eV] . . . . .   | 6.42 (6.41–6.43) | (fixed to Src1) | 6.38 (6.36–6.41) | 6.41 (6.37–6.45) | 6.40 (6.38–6.42) |
| Surface brightness<br>[ $10^{-8}$ ph cm $^{-2}$ s $^{-1}$ arcmin $^{-2}$ ] . . . . . | 6.5 (5.8–7.2)    | 5.9 (3.7–8.1)   | 6.6 (4.3–8.9)    | 2.3 (1.2–3.4)    | 3.2 (2.5–3.9)    |
| He-like Iron   |                  |                 |                  |                  |                  |
| Line center [eV] . . . . .   | 6.68 (6.67–6.69) | (fixed to Src1) | 6.67 (6.66–6.68) | 6.69 (6.67–6.71) | 6.68 (6.67–6.69) |
| Surface brightness<br>[ $10^{-8}$ ph cm $^{-2}$ s $^{-1}$ arcmin $^{-2}$ ] . . . . . | 11 (10–12)       | 12 (10–14)      | 17 (14–20)       | 10 (9–11)        | 11 (10–12)       |

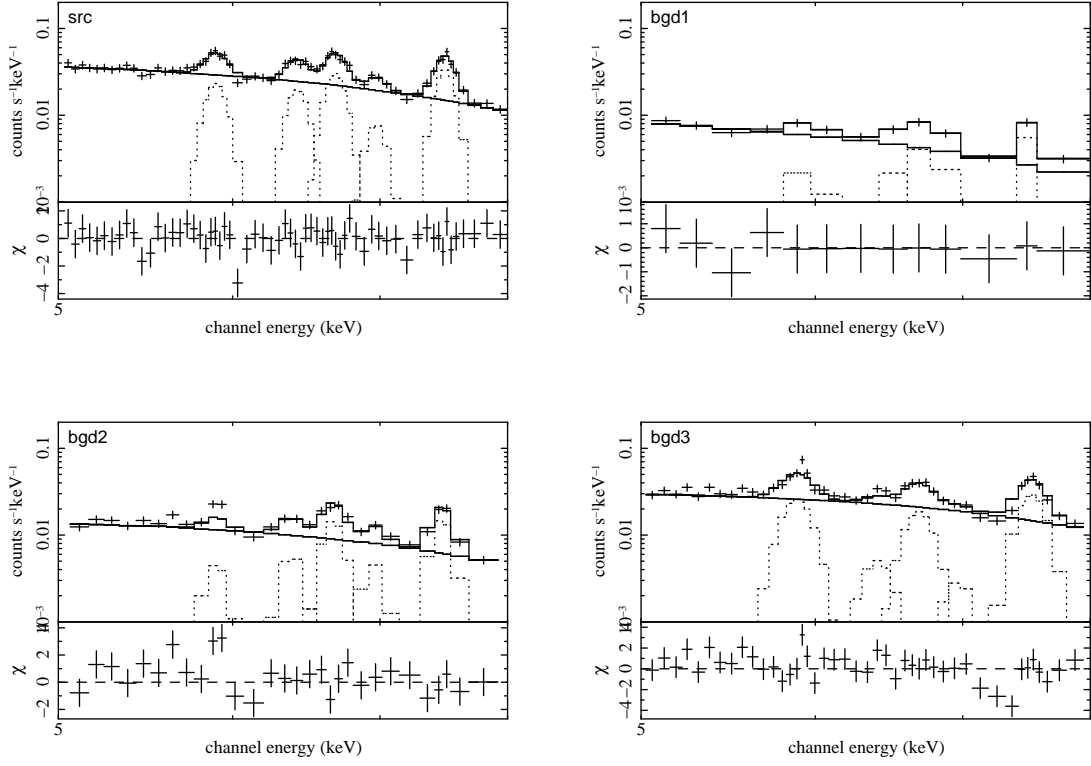


Fig. 3.— XIS spectra of src and bgd regions. Background photons were not subtracted. Solid and dotted lines represents the continuum and emission lines. Although the fittings were done with 4 XISs, only XIS0 data are plotted for convenience.

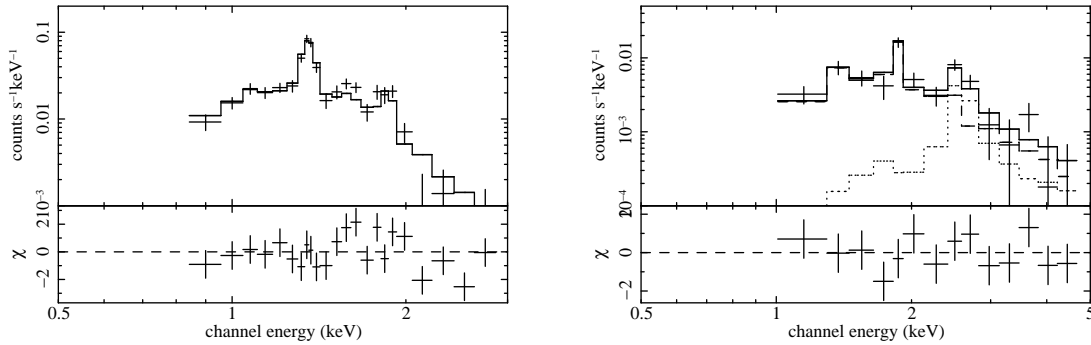


Fig. 4.— XIS Spectra of G359.0–0.9 (left) and G359.1–0.5 (right). Only XIS0 data are plotted for convenience. Solid and dashed lines represents the lower and higher temperature plasma models.



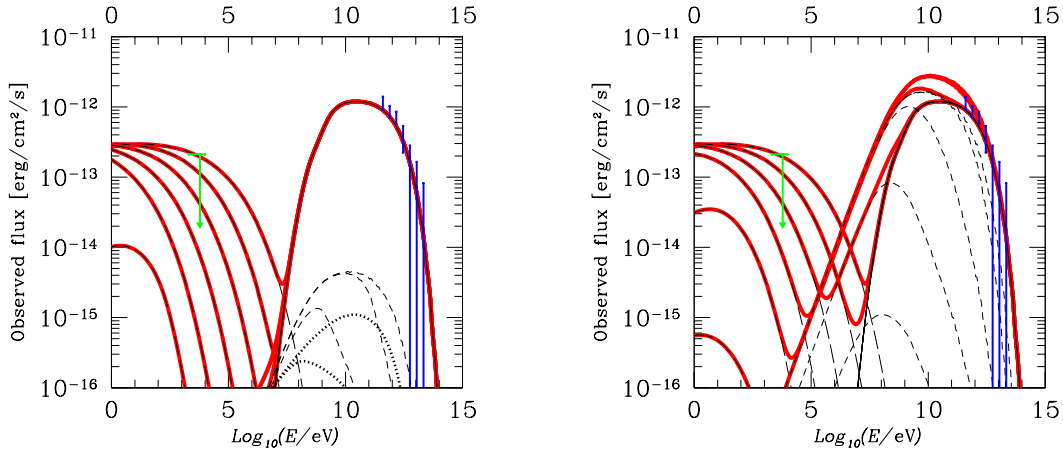


Fig. 5.— The wide-band  $\nu F_\nu$  spectra of the region A of HESS J1745–303 calculated by the hadronic gamma-ray emission model. The thick-solid line shows the total nonthermal flux. Thin-solid line corresponds to  $\pi^0$ -decay gamma-rays. The dotted, dashed, and long-dashed lines are for the inverse-Compton, bremsstrahlung, and synchrotron emissions from secondary electrons and positrons produced by charged pions. The left panel is for the low-target density model ( $n = 1 \text{ cm}^{-3}$ ), while the right is for the high-target density model ( $n = 5 \times 10^3 \text{ cm}^{-3}$ ). In calculating the synchrotron radiation of secondary electrons and positrons, the magnetic field strength is changed; 1 G, 100 mG, 10 mG, 1 mG, 100  $\mu\text{G}$ , and 10  $\mu\text{G}$  downward from right to left. In both panels, we assume that the primary proton spectrum is in the form of  $E^{-p} \exp(-E/E_{\text{max,p}})$  with an index  $p = 2.0$  and the cut-off energy,  $E_{\text{max,p}} = 18 \text{ TeV}$ .

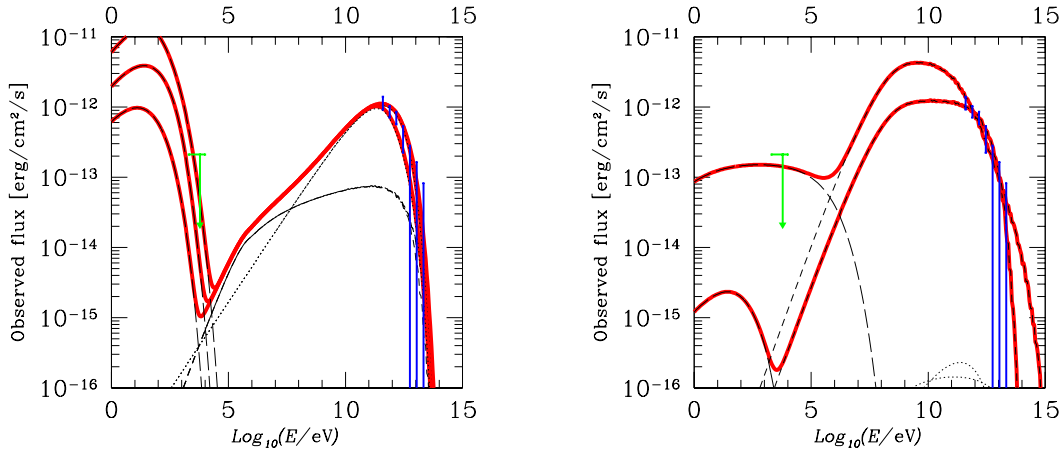


Fig. 6.— The wide-band  $\nu F_\nu$  spectra of the region A of HESS J1745–303 calculated by the leptonic gamma-ray emission model. The thick-solid line shows the total nonthermal flux. The dotted, dashed, and long-dashed lines are for the inverse-Compton, bremsstrahlung, and synchrotron emissions from primarily accelerated electrons. The left panel is for the low-target density model ( $n = 0.1 \text{ cm}^{-3}$ ). In calculating the synchrotron radiation of secondary electrons and positrons, the magnetic field strength is changed;  $12 \mu\text{G}$ ,  $6 \mu\text{G}$ , and  $3 \mu\text{G}$ , downward from right to left. The right panel is for the high-target density model ( $n = 5 \times 10^3 \text{ cm}^{-3}$ ). We consider two cases of  $B = 10 \mu\text{G}$  and  $100 \mu\text{G}$ . In both panels, we assume that the primary electron spectrum is in the form of  $E^{-p} \exp(-E/E_{\text{max,e}})$  with an index  $p = 2.0$  and the cut-off energy,  $E_{\text{max,e}} = 10 \text{ TeV}$ .

Table 3. Best-fit parameters of G359.0–0.9 and G359.1–0.5<sup>a</sup>.

|  | G359.0–0.9            | G359.1–0.5            |
|--|-----------------------|-----------------------|
| $kT_1$ [keV] .....                                       | 0.35 (0.32–0.38)      | 1.1 (0.7–2.0)         |
| Mg .....   | 1.4 (1.1–1.6)         | — <sup>b</sup>        |
| Si .....   | — <sup>b</sup>        | 1.9 (1.3–2.9)         |
| Fe .....   | 0.4 (0.2–0.6)         | — <sup>b</sup>        |
| $n_{e,t}$ [ $10^{11}$ cm <sup>-3</sup> s].....           | 2.3 (1.5–3.7)         | — <sup>c</sup>        |
| $kT_2$ [keV].....  | — <sup>d</sup>        | 2.0 (1.7–2.5)         |
| S .....  | — <sup>d</sup>        | (>40)                 |
| $N_H$ [ $10^{22}$ cm <sup>-2</sup> ].....                | 1.6 (1.5–1.8)         | 2.3 (1.6–2.5)         |
| Flux (2–10 keV) [ergs s <sup>-1</sup> cm <sup>-2</sup> ] | $7.1 \times 10^{-14}$ | $2.6 \times 10^{-13}$ |
| $\chi^2$ /d.o.f.....                                     | 109.7/70              | 64.0/41               |

<sup>a</sup>Errors indicate single parameter 90% confidence regions.

<sup>b</sup>Fixed to the solar abundance.

<sup>c</sup>Not determined.

<sup>d</sup>This component was not used for this SNR.

Table 4. Characteristics of molecular clouds

|   | Sgr B2 <sup>a</sup> | HESS J1745–303 <sup>b</sup> |
|---|---------------------|-----------------------------|
| $M_{MC}$ <sup>c</sup> [ $M_\odot$ ] ..... | $6 \times 10^6$     | $5 \times 10^4$             |
| $\theta$ [deg.] <sup>d</sup> .....        | 0.05                | 0.3                         |
| $D$ <sup>e</sup> [deg.].....              | 1.2                 | 0.7                         |

<sup>a</sup>Murakami et al. (2001).

<sup>b</sup>Aharonian et al. (2008).

<sup>c</sup>Mass of the molecular cloud.

<sup>d</sup>Angular size of the cloud from the direction of the GC.

<sup>e</sup>Angular separation from the GC to the cloud.